# The global frequency-wavenumber spectrum of oceanic variability estimated from TOPEX/POSEIDON altimetric measurements

Carl Wunsch and Detlef Stammer

Department of Earth, Atmospheric and Planetary Sciences, Massachusetts Institute of Technology, Cambridge

**Abstract.** Two years of altimetric data from the TOPEX/POSEIDON spacecraft have been used to produce preliminary estimates of the space and time spectra of global variability for both sea surface height and slope. The results are expressed in terms of both degree variances from spherical harmonic expansions and in along-track wavenumbers. Simple analytic approximations both in terms of piecewise power laws and Padé fractions are provided for comparison with independent measurements and for easy use of the results. A number of uses of such spectra exist, including the possibility of combining the altimetric data with other observations, predictions of spatial coherences, and the estimation of the accuracy of apparent secular trends in sea level.

## 1. Introduction

With more than 2 years of high quality sea surface elevation measurements now available from the TOPEX/POSEIDON altimetric spacecraft [*Fu et al.*, 1994; *Stammer and Wunsch*, 1994], it is possible to calculate the global average absolute and time-dependent elements of the global ocean circulation. From these fields one can now estimate the corresponding three-dimensional frequency/wavenumber spectra. Although estimates representing the global average are not a substitute for detailed regional ones, the global average provides a reference against which to measure the myriad of regional variations and is a fundamental element in a description of the ocean circulation and its variability. It also provides, among other possibilities, a simple average test of the skill of the current generation of global-scale general circulation models. The availability of a spectrum would permit the quantitative calculation of the statistical significance of such important values as estimates of global mean sea level and its rate of change. The analogy to the widely useful internal wave spectrum of *Garrett and Munk* [1972] will be apparent.

A number of one- and two-dimensional spectra from GEOSAT are available [e.g., *Wunsch*, 1991; *Stammer and Böning*, 1992]. *LeTraon et al.* [1994], *Stammer and Böning*, [1995] and A. Fabrikant et al. (Statistical analysis of spatio-temporal variations of sea surface height observed by Topex altimeter, unpublished manuscript, 1995) have used TOPEX/POSEIDON data; but, with the exception of *Wunsch* [1991], these results are mainly regional in character, and those from GEOSAT data are intrinsically much less accurate than those it is now possible to obtain.

We will here produce a preliminary estimate of the global frequency/wavenumber spectrum of two years of global temporal variability as seen by TOPEX/POSEIDON. At the present time, the wavenumber content of the time mean and absolute fields is dominated by uncertainty in the estimates of the geoid (the gravitational equipotential describing the sea surface shape of a resting ocean), and thus we confine ourselves here to the time variability; that is, we omit discussion of the wavenumber content of the time average fields. The results are labeled "preliminary" for a number of reasons: the much longer records expected eventually to be available will improve both the frequency resolution and the statistical reliability; and improvements are still being made in the data sets. However, we also will postpone to a later paper a discussion of propagation in the spectrum, a discussion which is much more complex than is required here.

The sea surface topography is related directly to the potential energy of the circulation; from its horizontal derivatives one can estimate the kinetic energy of the circulation. A full discussion involves the partitioning within the water column of the motions reflected in sea surface pressure fields, and that partitioning is intimately related to the frequency/wavenumber spectrum itself.

TOPEX/POSEIDON data were used from the period December 11, 1992, to December 5, 1994 (repeat cycles 9-81; earlier cycles were omitted because of lingering questions about pointing errors during that period. In practice, analyses including cycles 2-8 produced results almost indistinguishable from the ones we will show.) The data were edited and corrected as discussed by

*Stammer and Wunsch* [1994] and *King et al.* [1994], with the exception that the tide correction provided by the University Texas/Center for Space Research Group [*Ma et al* 1994] in their version 2.0 was substituted for the one provided by the TOPEX/POSEIDON Project. The spacecraft is in an orbit which repeats its trajectory over the Earth with a period of 9.91 days (these will be referred to, for brevity, as "10-day" repeat cycles). Each 10-day data set was averaged in $2° \times 2°$ bins to produce a map of estimated "absolute" sea surface topography, $S(\theta, \lambda, t)$, relative to the geoid ($\theta, \lambda$ are colatitude and longitude, respectively; and $t$ labels the particular 10-day interval). Plate 1 depicts the estimated anomaly $S'(\theta, \lambda, t) = S(\theta, \lambda, t) - \bar{S}(\theta, \lambda)$ as a single, 10-day "snapshot" during the period March 10–20, 1993 (repeat 18), relative to the 2 year mean. These temporal anomalies, $S'(\theta, \lambda, t)$, and the corresponding fields in the 72 other 10-day periods spanning the 2 years of data are the focus of this paper. (We assume that the 10-day repeat cycle temporal sampling by TOPEX/POSEIDON with the data then averaged in $2° \times 2°$ bins is adequate to depict the bulk of the low-frequency oceanic temporal variability. The hypothesis cannot be correct in detail, and the extent to which energetic fluctuations occur on timescales short compared with 10 days has to be examined separately and is discussed below. Because of the "diamond" pattern of sampling produced by an orbiting spacecraft, the degree of averaging in each $2° \times 2°$ bin is not completely uniform. However, the results reported below support the hypothesis that any residual spatial or temporal aliasing from this inhomogeneity is likely to be very small.) Although a complete error budget for the measured variability is not yet available, a large amount of internal evidence suggests that the data have an absolute accuracy approaching 3 cm rms and a precision of about 2 cm rms; the mean-square variability discussed here is approximately 92 cm$^2$.

In pursuing a frequency/wavenumber description, one immediately encounters the question of a representational basis. The most natural form is

$$S(\theta, \lambda, t) = \sum_n \sum_m \alpha_{nm}(t) F_{nm}(\theta, \lambda), \qquad (1)$$

where $\alpha_{nm}(t)$ are time dependent coefficients and $F_{nm}(\theta, \lambda)$ express the geographical dependence. In a Cartesian system, ordinary sines and cosines in both space and time would be used; on a water-covered globe, spherical harmonics are the natural basis set for the spatial coordinates. However, the Earth is not water-covered, and there is no completely natural or obvious system of representation. At least four candidate basis functions, $F_{nm}(\theta, \lambda)$, present themselves as follows. (1) One can adopt any basis orthogonalized over the ocean, including a Gram-Schmidt orthogonalization of the spherical harmonics (a version of this approach is discussed by *Hwang* [1993]). (2) The ordinary associated Legendre functions of the first kind, $P_{nm}(\cos\theta)$, $n, m$ integers, do not form a complete set over a fraction of a sphere, and the associated Legendre functions of the second kind, $Q_{nm}(\cos\theta)$, are required

too. Using both, one can find such a complete set (see *Thompson and Tait* [1912], or *Haines* [1985], who considers a hemispherical region). (3) The empirical orthogonal functions of either the altimetric data itself or those of a reasonable dynamical model could be used. (4) One can use the spherical harmonics, $Y_{nm}(\theta, \lambda)$, based upon $P_{nm}$ either by finding their coefficients by least squares (the spherical harmonics lose their orthogonality over a domain restricted to the ocean) and ignore the issue of completeness; or one can define nominal values over the continents and represent the global domain including these artificial regions.

Arguments can be made for any of these approaches (and there may well be others), but none seems completely compelling. In this present attempt, for a number of reasons we have opted for (4), in the form of zonal and time average altimetric values over the continents. With this approach the wavenumber content of the basis function $F_{nm}(\theta, \lambda) = Y_{nm}(\theta, \lambda)$ is readily described in terms of the known behavior of these functions; fast transform software for determining the coefficients $\alpha_{nm}$ is available; similar software is available for quasi-analytical computation of the derivatives of $S$ so as to determine the corresponding coefficients of the derived geostrophic velocity fields; the atmospheric forcing fields occupy the entire spherical domain, and for them the $Y_{nm}$ are clearly the natural basis functions. Apart from some normalization details, this representation is the one used by *Wunsch* [1991], but we make no claim that we have made the best possible choice.

## 2. The Representation

Spherical harmonics are a maze of differing normalization conventions (a standard reference is *Hobson* [1955]). Here we will use the so-called fully normalized version familiar in quantum mechanics. *Jackson* [1962] provides a good discussion, and we roughly follow his notation. To make unambiguous the notational and normalization conventions used, the definitions are written out explicitly in the appendix.

The complex coefficients in the representation (1) were computed by defining land values as the time average of the zonal mean absolute topographies, $S(\theta, \lambda, t)$, of repeat cycles 9-81, as a means of minimizing the Gibbs effects which would otherwise occur at the land-ocean boundaries. Poleward of $66°$, $S$ was set to the zonal average at $66°$. Small along-track temporal gaps over the ocean were filled with the time average at the particular position. The result is a set of uniformly gridded $2° \times 2°$ values which were analyzed using the software described by *Swarztrauber and Adams* [1987], thus producing an expansion in each 10-day period of the form (1) complete to degree $n = 90$. Note that the expansion is of the absolute topography $S$, not $S'$. The result is $(90 + 1)^2 = 8281$ separate time series $\alpha_{nm}(t)$, $-n \leq m \leq n$, $0 \leq n \leq 90$ with nonzero means. A simple check on the results was applied, confirming satisfaction of the Parseval theorem,

$$\int\int S(\theta,\lambda,t)^2 \sin\theta d\theta d\lambda = \sum_{n=0}^{90}\sum_{m=-n}^{n} |\alpha_{nm}(t)|^2, \quad (2)$$

with the two sides of this equation agreeing with discrepancies less than 0.07% for all $t$. The along-track gap filling and use of land values are simple solutions which are not claimed to be optimal; but comparisons of spectra from along-track data (discussed below) with those computed from the interpolated, gridded, partially land data, show no discrepancies, suggesting that the procedures do not introduce any significant distortions into our results.

Because of the focus on the variability, the time average $\bar\alpha_{nm}$ was removed from each of these time series, producing $\alpha'_{nm}(t) = \alpha_{nm}(t)-\bar\alpha_{nm}$, and the mean square was computed over time to produce the mean square coefficients,

$$r'_{nm} = \frac{1}{73}\sum_{t=9}^{81} |\alpha'_{nm}(t)|^2, \quad (3)$$

whose logarithm is displayed in Figure 1. Because $S$ and $S'$ are real, one has $\alpha'_{n,-m} = \alpha'^{*}_{nm}$. (One could equally well directly compute $\alpha'_{nm}(t)$ from the gridded anomalies; but for other purposes, we wished to have

the spherical harmonic analysis through time of the total field.) Most of the variability is concentrated at the longest meridional scales (near $n = 0$) and at zonal wavenumbers which are slightly smaller than $n = m$, showing a tendency to isotropy, but with a longer zonal than meridional scale at high wavenumbers. (The various scales are most readily inferred from the asymptotic form [Stegun, 1965, equation (8.10.7)],

$$Y_{nm}(\theta,\lambda) =$$

$$\sqrt{\frac{(2n+1)(n-m)!}{4\pi(n+m)!}\frac{(n+m)!}{\Gamma(n+3/2)}}\left(\frac{\pi}{2}\sin\theta\right)^{-1/2}$$

$$\times \cos[(n+1/2)\theta - \pi/4 + m\pi/2]e^{im\lambda}$$

$$+O(n^{-1}) \quad (4)$$

for $0 \le m \le n$, that is, for large $n$ the wavenumbers $k_n$ represented by each degree $n$ are approximately (up to the factor $(\sin\theta)^{-1/2}$) $k_n = \sqrt{n^2+m^2}/a_e$, where $a_e$ is the mean Earth radius. The range for fixed $n$ is $n/a_e \le k_n \le \sqrt{2}n/a_e$.)

Each of the $\alpha'_{nm}(t)$ was Fourier analyzed to produce the corresponding function in the frequency domain $\hat\alpha'_{nm}(\sigma)$ and the frequency periodogram,

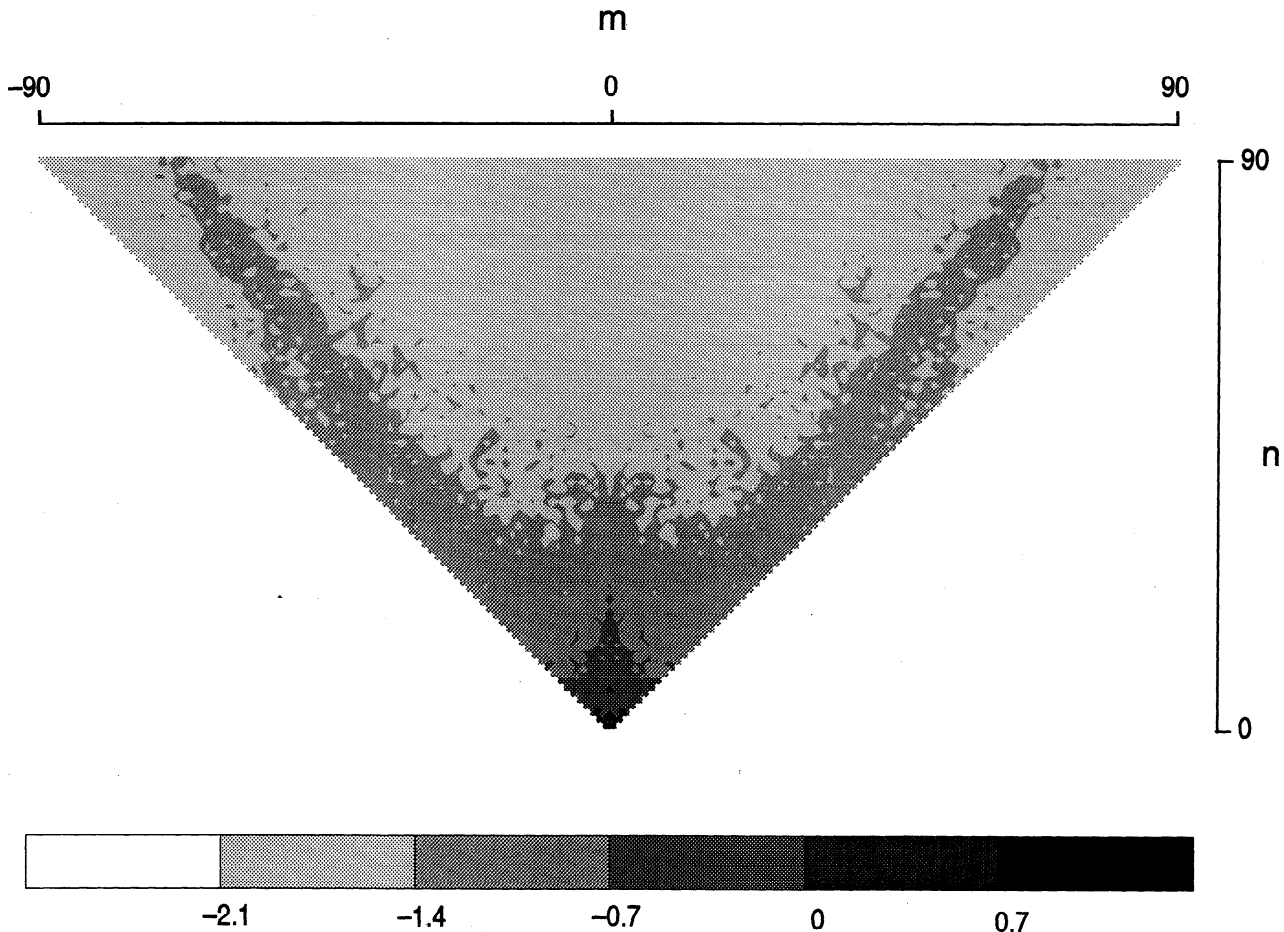$$\Phi'_{nm}(\sigma) = |\hat\alpha'_{nm}(\sigma)|^2. \quad (5)$$



Figure 1. Time average degree variances as a function of $n, m$ : $1/N\sum_{t=1}^{N}|\alpha'_{nm}(t)|^2 \equiv r'_{nm}$. If the field were strictly isotropic, the contours would run horizontally.

The $n = m = 0$ term is the periodogram of the estimate of global average sea level, whose behavior has been discussed in detail by *Nerem* [this issue], and so we will not dwell on it here, although it is included in our results as simply another spherical harmonic coefficient.

The Parseval theorem, when applied to the anomalies and the $\alpha'_{nm}$, was incompletely obeyed. The explanation appears to be that given by *Swartztrauber* [1979], whose algorithm we are using. In particular, he demonstrates that the discrete spherical harmonic expansion on the sphere is not exact (in contrast to the discrete Cartesian Fourier transform) but rather is a least squares fit. The result is that the original field need not be reproduced exactly by the inverse transform, and there is some aliasing of wavenumbers. We will show in the results below, however, that these problems appear insignificant.

The frequency-degree-order periodogram, (5), is a three-dimensional stochastic surface and difficult to plot and interpret. We will thus begin examining some simpler results derived from it. Suppose that the field $S'(\theta, \lambda, t)$ were homogeneous and isotropic on the surface. It then follows in comparatively straightforward fashion [*Yaglom*, 1961; *Jones*, 1963; *Kaula*, 1967] that the coefficients satisfy

$$< \alpha'_{nm}(t)\alpha'_{n'm'}(t) > = a_n^2(t)\delta_{nn'}\delta_{mm'} \quad (6)$$

$$< \hat{\alpha}'_{nm}(\sigma)\hat{\alpha}'_{n'm'}(\sigma)^* > = |\hat{a}_n(\sigma)|^2\delta_{nn'}\delta_{mm'} \quad (7)$$

where the brackets denote a hypothetical ensemble average. The important point in (6) and (7) is that the covariance is independent of $m$, depending only upon the degree $n$. Under these circumstances, if the expected value of the periodogram (5) is summed on $m$,

$$\Psi'(\sigma, n) = < \sum_{m=-n}^{n} \Phi'_{nm}(\sigma) >$$

$$= < \sum_{m=-n}^{n} |\hat{\alpha}'_{nm}(\sigma)|^2 > = (2n+1)\hat{a}_n^2(\sigma) \quad (8)$$

which are the frequency-dependent "degree variances" shown in Figure 2a. (We will use the notation $\Psi$ for quantities derived from the periodogram $\Phi$ by summing over one or more of the three variables $n, m, \sigma$, and $\Gamma_i$ for quantities summed over two indices to produce one-dimensional degree variance $\Gamma_d$, frequency $\Gamma_t$, or wavenumber $\Gamma_s$ spectra. These symbols should not be confused with that for the gamma function $\Gamma$.) The result in (8) can be shown to be independent of the choice of coordinate system and in the present situation defines the spectrum of an equivalent homogeneous and isotropic process. Plate 1 and Figure 1 show that this description of the real ocean is very approximate. The result in Figure 2a is "reddish" in both frequency and wavenumber, with the weak highest peak associated with the annual variability. A second conspicuous ridge occurs centered near a period of 60 days and is a residual tidal model error of the semidiurnal tides, aliased to this period by the 10-day sampling.

To produce some statistical stability in this result, values in frequency were averaged over five neighboring components to produce an approximate 10 degrees-of-freedom power spectral density estimate $\bar{\Psi}'(\sigma, n)$ (Figure 2b) (no wavenumber averaging was done, however). The excess energy corresponding to the semidiurnal tides was removed prior to the averaging in Figure 2b.
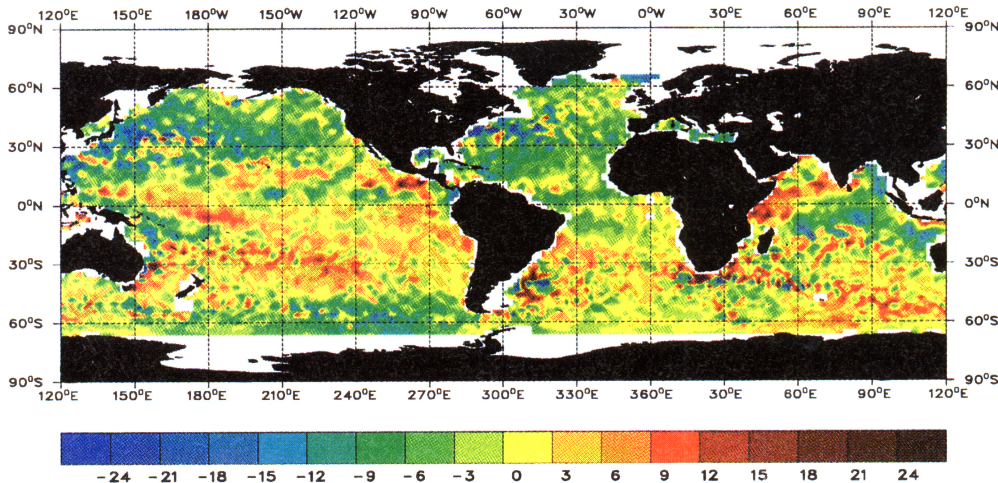


**Plate 1.** Example of a 10-day "snapshot" (from repeat cycle 18, March 10, 1993, to March 20, 1993) of the deviation of surface topography from the 2-year mean of TOPEX/POSEIDON data. The sequence of 10-day maps represents the ocean variability as analyzed here using spherical harmonics. The eye is attracted to the smaller scales which dominate the slope spectrum. Scale is in centimeters.
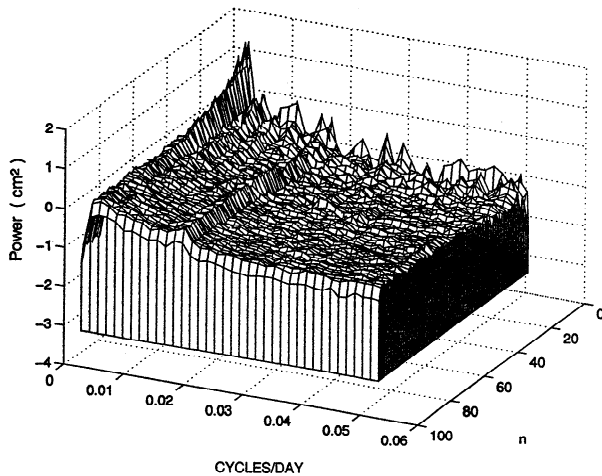
**Figure 2a.** Periodogram of the degree variances $a_n(\sigma)^2(2n+1) \equiv \sum_{m=-n}^{n} |\hat{\alpha}'_{nm}(\sigma)|^2$. The ridge of excess energy, attributed to errors in the semidiurnal tide models, is apparent near a period of 60 days.
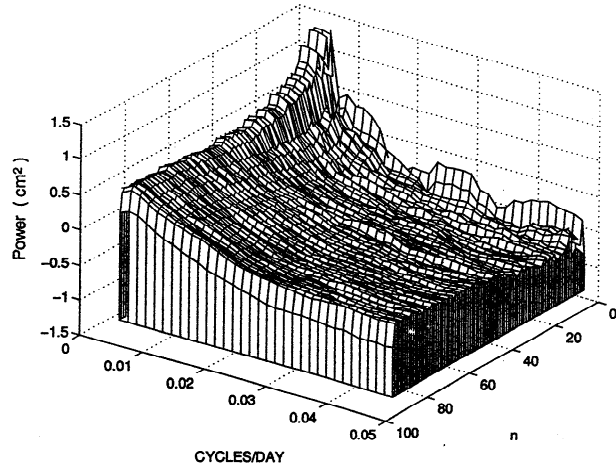


**Figure 2b.** Power density (smoothed in frequency alone) estimate of the degree variances as a function of frequency. The tidal energy was removed by interpolating across the 60-day band. To avoid edge effects, the two highest and lowest frequencies were dropped.

## 3. The Frequency and Wavenumber Spectra

### The Frequency Spectrum

Figures 2a and 2b are still fairly complex. To further elucidate their structure, they were summed over all degrees $n$ to produce the frequency power density spectrum estimate,

$$\Gamma_t(\sigma) = \frac{1}{4\pi} \sum_{n=0}^{90} \Psi'(\sigma, n), \qquad (9)$$

in Figure 3a. (The factor $1/4\pi$ has been introduced to produce a power density spectrum numerically equivalent to that obtainable from analysis of the time series at one or more geographical locations. It arises because the fully normalized spherical harmonics integrate to 1 over the unit sphere, whose area is $4\pi$.) The maximum value in $\Gamma_t$ occurs at the annual period. The version of Figure 2a computed by *Wunsch* [1991] from GEOSAT data is qualitatively consistent with it, accounting for normalization differences and the presence of a strong orbital error peak in that earlier result. A slight upturn in estimated energy density is visible in Fig. 3a at the shortest period (20 days), which is apparently associated with a small residual error in correcting the weak semidiurnal constituents $L_2, \mu_2$.

A representative, approximate 95% confidence interval is shown, computed under the assumption that $\Psi'(\sigma, n)$ is a $\chi^2_\nu$ variate with $\nu = 2 \times (2n+1)$ degrees of freedom (the sum on $m$ in (8) of the $|\hat{\alpha}'_{nm}(\sigma)|^2$, assumed uncorrelated and with each composed of an uncorrelated real and imaginary part). Formally, the sum on $n$ then produces $2 \times \sum_{n=0}^{90}(2n+1) = 2 \times 8281$ degrees of freedom if one had spatial white noise over a complete sphere. The use of land values produces dependencies among the spherical harmonic coefficients, and the field is not white. Consequently, a rigorous determination

of the confidence limits has not been possible, and we have assumed that the induced dependencies reduce the degrees of freedom to about 1/3 the hypothetical maximum value. The result may be optimistic, but note that much of the small-scale structure visible is actually residual aliased tidal lines.
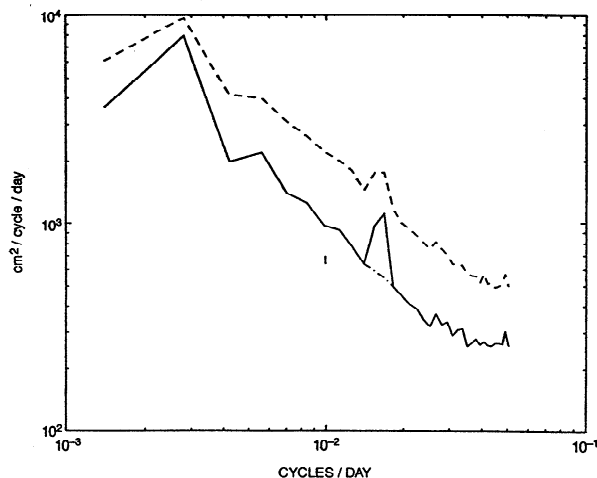


**Figure 3a.** Frequency power density spectrum computed by summing figure 2a over all degrees (wavenumbers) $n$, with conversion to a power per unit frequency band (solid line). Also shown (dashed line) is the frequency power density spectrum computed as an average of the periodograms of sea level at several thousand subsatellite points, each treated as an ordinary time series. The semidiurnal tidal error is conspicuous in both. Gridding of the data accounts for the reduced energy as seen by the spherical harmonic analysis. Also shown, as a dash-dotted line, is the interpolation across the tidal alias band. Other weak aliased tides produce some of the remaining small peaks, e.g., near 20 days. An approximate 95% confidence interval for the along-track spectrum is ±3% of the displayed spectral values (see text).

Also shown in Figure 3a is the frequency power density spectrum estimated by computing the average periodograms from time series of sea level variability at each of about 58,215 points at fixed locations every 60 km along the subsatellite track. If these time series were independent (they are not), we would have about $2 \times 58,215$ degrees of freedom. In practice, the number of degrees of freedom was assumed to be the same as in the spherical harmonic result. The energy level is higher across the entire frequency band from the fixed-location time series than from the spherical harmonics. The energy difference corresponds to that removed by the gridding onto the $2° \times 2°$ grid for an rms difference of 6.6 cm. The peak centered near a period of 60 days in both spectra are the aliased semidiurnal tidal components $M_2$ and $S_2$, incompletely removed from the results by the tidal model. The peak corresponds to an rms value of 1.3 cm, relative to the background continuum. (All displayed one-dimensional spectral densities have been normalized so that when multiplied by the bandwidth, the resulting power from any unit amplitude sinusoid present would be 1/2, producing an rms amplitude of $\sqrt{2}/2$; but owing to tapering of the various time series, the resulting value is reduced by an approximate factor of $1/1.1$. The rms amplitudes quoted here have been multiplied by 1.1 for a slightly more accurate estimate.) The residual background continuum after removal of the apparent tidal peak has a value of about 1.1 cm rms (in a bandwidth of 1 cycle/yr) and represents energy which should not be included in any tidal model. In Figure 2b and in all results based upon the spherical harmonic analysis, the values of $\hat{\alpha}'_{nm}(\sigma)$ were linearly interpolated across the 60-day tidal band to remove the excess tidal energy. The background continuum is higher near 60 days than it is near 12 hours, rendering the tidal determination from an altimeter more difficult, in this particular sense, than it is from a tide gauge sampling at a typical rate of once per hour.

Figure 3b displays $\Gamma_t(\sigma)$, interpolated across the tidal alias band and extended to frequencies above the 1 cycle in 20 days cutoff of the altimetric results, by using estimates from the Honolulu and Bermuda tide gauge records corrected for atmospheric load fluctuations. Apart from the annual peak the spectrum is "red," obeying an approximate relationship of

$$\Gamma_t(\sigma) = 21.3\sigma^{-1}, 1.4 \times 10^{-3} \leq \sigma \leq 5 \times 10^{-2}$$
$$\Gamma_t(\sigma) = 1.06\sigma^{-2}, 5 \times 10^{-2} < \sigma \qquad (10)$$

shown in Figure 3b ($\sigma$ is in circular, not radian, units of cycles per day, and $\Gamma_t$ is in square centimeters per cycle per day.) The annual peak is about 2.8 cm rms, relative to the background continuum of about 3.0 cm rms (which was estimated from the energy density at the next higher and lower frequencies in the spectral estimate). A weak semiannual peak is present, probably somewhat contaminated by residual error from the aliased $K_1$ tide. The total rms variability between 2 years and 20 days, exclusive of the 60-day band semidiurnal tidal error but including the annual period, is
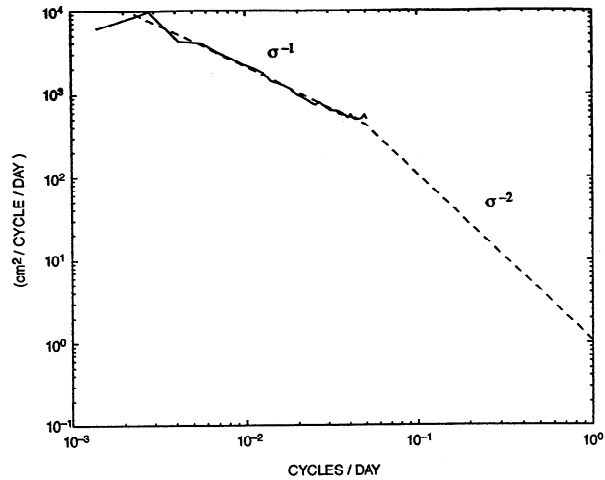


**Figure 3b.** Frequency power density from the along-track data in Figure 3a, but interpolated across the tidal band and showing a high-frequency extension. The extension was obtained from the Bermuda [*Wunsch*, 1972] and Honolulu [*Munk and Cartwright*, 1966] tide gauges corrected for a static atmospheric load and should be regarded only as a rough schematic of the actual, unknown form. The 95% confidence limit on the solid curve is again about ±3% of the value shown.

about 9.7 cm rms (27 cm peak to trough). The high-frequency extension of (10) shown in Figure 3b is simply a plausible suggestion based upon tide gauge results (*Munk and Cartwright* [1966] for Hawaii and *Wunsch* [1972] for Bermuda) but is intended only as a crude placeholder; a global analysis of pressure-corrected tide gauge records will be required to produce a more accurate version, and even then, the spatial coverage will undoubtedly prove less than desirable.

Because the assumption of homogeneity is a fiction convenient as a reference state, it is important to examine the variability in the space as well as the wavenumber domains. Plate 2 shows the rms sea surface height variability (in centimeters) during the 2 year period and after averaging in $2° \times 2°$ geographical areas. The computation was done using the along-track, rather than the gridded data to retain the complete spectrum of wavenumbers. Similar figures have been published before; using the higher quality TOPEX/POSEIDON data, however, leads to a decrease in the ambient variability in the bulk of the quiescent subtropical oceans and reveals variability associated with major currents with better spatial coherence. The extreme quiescence of the South Atlantic and eastern South Pacific in the latitude band from about 20°-30°S is remarkable.

Oceanic variability is broadband, including seasonal and interannual variability as well as the mesoscale, and so Plate 2 is not simple to interpret. To obtain some insight into the timescales involved, we band-pass filtered the (local) TOPEX/POSEIDON time series to form separate maps for the variability on timescales shorter than 150 days, the timescale of the oceanic mesoscale [*Richman et al.*, 1977], and longer. Plates 3a and b display the rms variability in the so-called eddy-
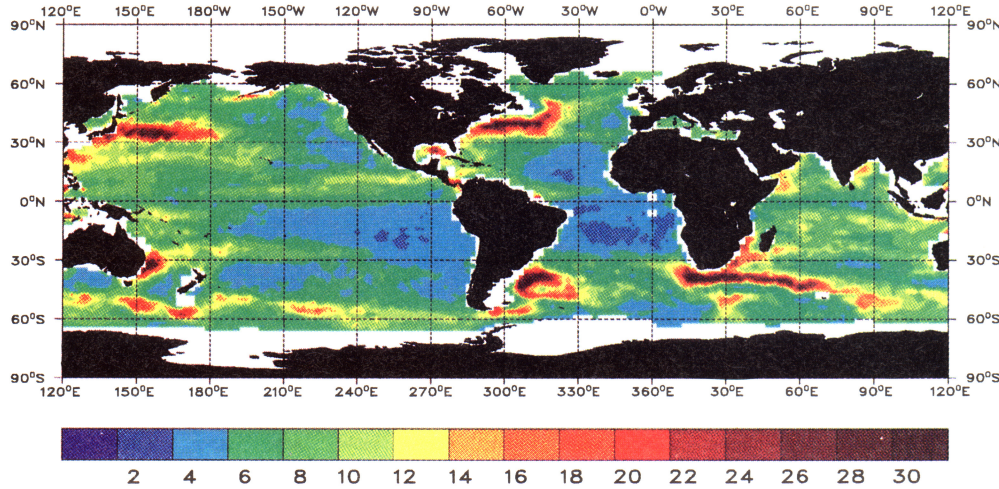
**Plate 2.** Root-mean-square sea surface variability (in centimeters) about the temporal mean as a function of position from the 2 years of data (repeat cycles 9-81, December 11, 1992, to December 5, 1994) computed from the along-track data. Note large regions of very small values.

containing band and for the periods longer than 150 days in the so-called interannual band (including the seasonal changes). The percentage contribution of the eddy-containing band to the total variance is shown in Plate 3c. Globally, about half of the variance lies in periods longer than those of the eddy-containing band. In particular, the subtropical gyres and frontal structures such as the Azores Current are dominated by variability on the longer periods and not by the mesoscale. Plate 3b (see also *Stammer and Böning* [1995]) shows that most of the variability in the intense current systems occurs on short timescales. Enhanced eddy variability is visible along many boundaries; for example, the Madagascar Current, the Agulhas Retroflection system, and the Benguela Current are all associated with intense short-period variability. In addition, a distinct geographical pattern of enhanced eddy activity can be found which, e.g., in the Atlantic Ocean, leads to an interesting pattern in Plate 3c, almost symmetric about the equator with a high percentage along the North and South Equatorial Currents and on the equator. Variability on increasingly short timescales is present in high latitudes. The Pacific has a similar distribution, although not as distinct as in the Atlantic.

### The Degree Variance Spectrum

The sum over all frequencies in Figure 2a defines the total degree variances,

$$\Gamma_d(n) = \sum_\sigma \Psi'(\sigma, n), 1 \leq n \leq 90 \tag{11}$$

depicted in Figure 4 (solid line) in units of square centimeter. The minor low-degree peaks are not statistically significant, and the result is similar to but much more accurate than that of *Wunsch* [1991], who plotted the equivalent of $\hat{a}_n^2 = \Gamma_d(n)/(2n + 1)$. Otherwise, the general character of $\Gamma_d(n)$ is a nearly white spectrum from the largest scale (40,000 km wavelength) to

the high-degree (high wavenumber) cutoff near wavelengths of about 400 km. Here, for descriptive purposes, wavelength is taken to be $2\pi a_e/n \approx 40,000 \text{km}/n$. The high-wavenumber extension (dashed curve) in Figure 4 is discussed below.

### One-Dimensional Spatial Spectrum

The degree variance spectrum is somewhat unfamiliar, and there is reason, in any case, to seek an estimate of the wavenumber power density spectrum of sea level along linear tracks. To proceed, we continue to examine an equivalent homogeneous and isotropic field. Under this assumption the wavenumber spectrum computed from along-track data from all great circles on the sphere will be statistically identical. In particular, the equator, $\theta = \pi/2$, is such a great circle, and we can therefore evaluate

$$S(\pi/2, \lambda) = \sum \sum \alpha_{nm} Y_{nm}(\pi/2, \lambda)$$
$$= \sum \sum \alpha_{nm} \sqrt{\frac{(2n+1)(n-m)!}{4\pi(n+m)!}} P_{nm}(0)e^{im\lambda};$$
$$\tag{12}$$

but [*Stegun*, 1965],

$$P_{nm}(0) = \frac{\Gamma((n+m+1)/2)}{\Gamma((n-m)/2+1)} \frac{2^m}{\sqrt{\pi}} \cos[\frac{\pi}{2}(n+m)] \tag{13}$$

for $m > 0$, and

$$P_{nm}(0) = (-1)^{|m|} \frac{(n-|m|)!}{(n+|m|)!} P_{n|m|}(0) \tag{14}$$

for $m < 0$, so that using $q! = \Gamma(q+1)$, (this $\Gamma$ is the gamma function) and the definition of the $Y_{nm}$,
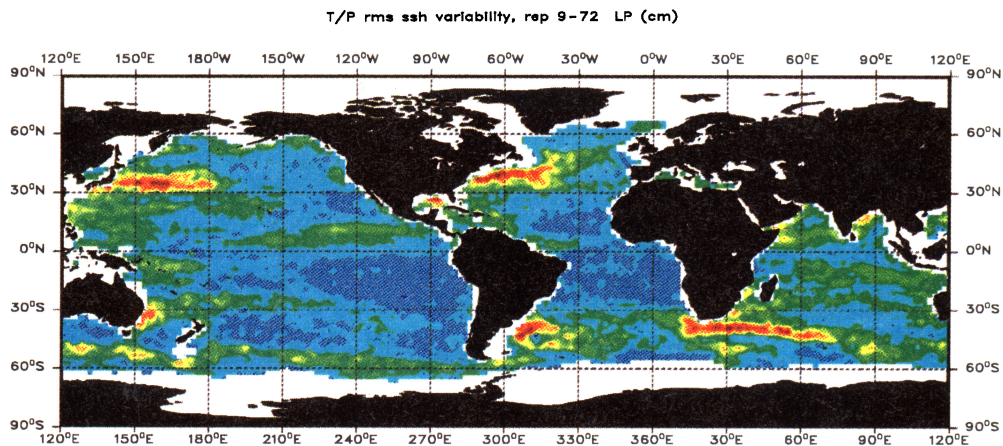
T/P rms ssh variability, rep 9-72  LP (cm)

**Plate 3a.** Root-mean-square sea surface height variability as a function of position for timescales (periods) exceeding 150 days (in centimeters).
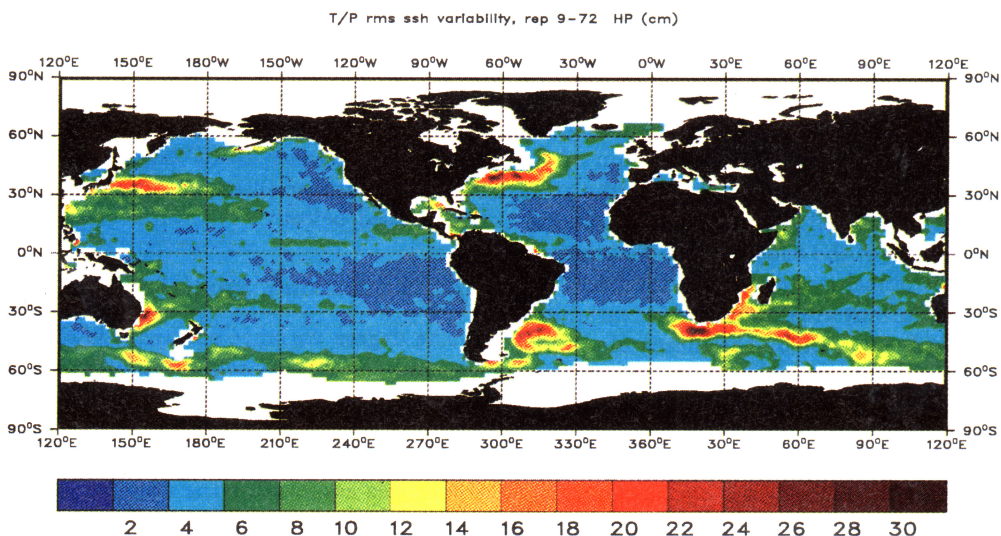
T/P rms ssh variability, rep 9-72  HP (cm)

**Plate 3b.** Root-mean-square sea surface height variability (in centimeters) as a function of position for timescales less than 150 days.

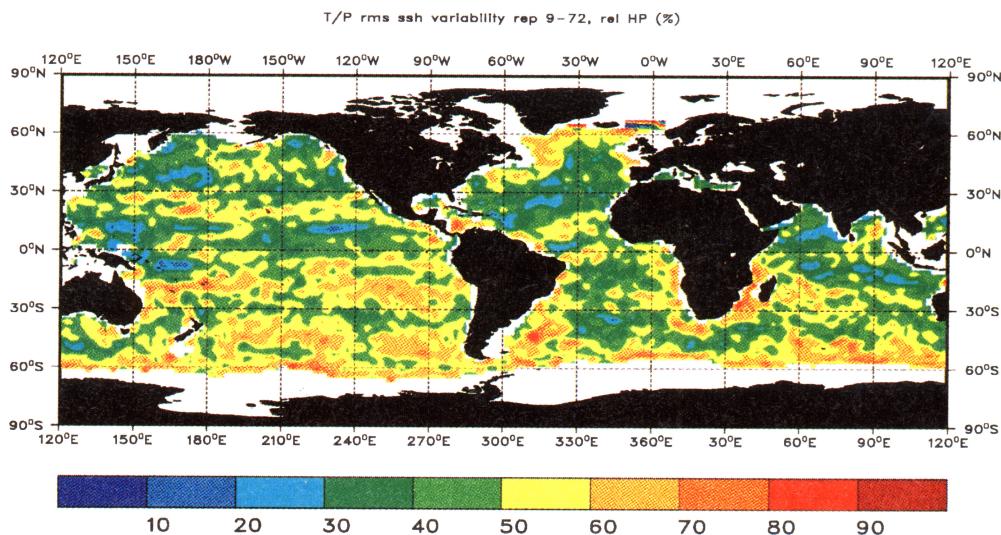T/P rms ssh variability rep 9-72, rel HP (%)

**Plate 3c.** Percentage of the total 2 year variance represented by the eddy-containing band, i.e., the relative proportion represented by Plate 3b.
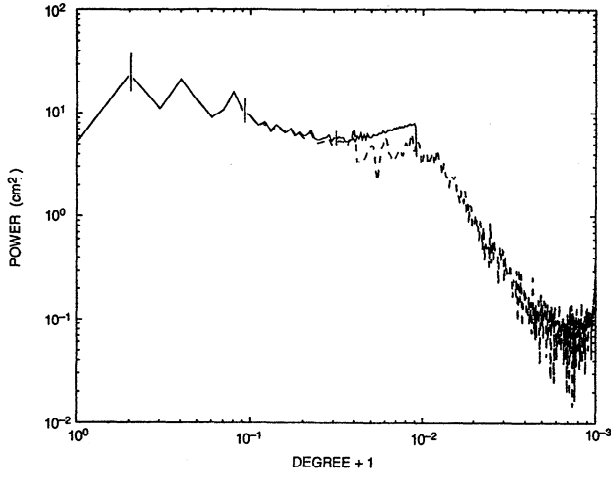
**Figure 4.** Degree variance power spectrum (not power density) computed by summing Figure 2a over all temporal frequencies (solid line). Dashed line shows the inferred extension from the along-track wavenumber spectra (Figures 5a and 5b), using (17). The upturn at the highest values of $n$ in the solid curve is an artifact of truncating the wavenumber spectrum (see text). Some representative approximate 95% confidence limits were calculated by assuming $2 \times (2n+1)$ degrees of freedom for each value $n$ but that the sum over the 37 frequency estimates produces only about another factor of 4 degrees of freedom owing to the power law dependence of the frequency spectrum.

$$S(\pi/2, \lambda, t)$$

$$= \sum_{n=0}^{90} \sum_{m=0}^{n} \alpha_{nm} \sqrt{\frac{(2n+1)\Gamma(n-m+1)}{4\pi(n+m)!}}$$

$$\times \frac{\Gamma[(n+m+1)/2]}{\Gamma[(n+m)/2+1]} \frac{2^m}{\sqrt{\pi}} \cos[\frac{\pi}{2}(n+m)] e^{im\lambda}$$

$$+ \sum_{n=0}^{90} \sum_{m=-n}^{-1} \alpha_{nm} \sqrt{\frac{(2n+1)\Gamma(n-|m|+1)}{4\pi\Gamma(n+|m|+1)}}$$

$$\times \frac{\Gamma[(n+|m|+1)/2]}{\Gamma[(n+|m|)/2+1]} \frac{2^{|m|}}{\sqrt{\pi}} (-1)^m \cos[\frac{\pi}{2}(n+|m|)] e^{im\lambda} \tag{15}$$

which, if Fourier transformed around the Earth, gives

$$\hat{S}(\pi/2, k, t)$$

$$= \sum_{n=0}^{90} \sum_{m=0}^{n} \alpha_{nm} \sqrt{\frac{(2n+1)\Gamma(n-m+1)}{4\pi\Gamma(n+m+1)}}$$

$$\times \frac{\Gamma[(n+m+1)/2]}{\Gamma[(n+m)/2+1]} \frac{2^m}{\sqrt{\pi}} \cos[\frac{\pi}{2}(n+m)]\delta(k-m)$$

$$+ \sum_{n=0}^{90} \sum_{m=-n}^{-1} \alpha_{nm} \sqrt{\frac{(2n+1)\Gamma(n-|m|+1)}{4\pi\Gamma(n+|m|+1)}}$$

$$\times \frac{\Gamma[(n+|m|+1)/2]}{\Gamma[(n+|m|)/2+1]} \frac{2^{|m|}}{\sqrt{\pi}} (-1)^m$$

$$\times \cos[\frac{\pi}{2}(n+|m|)]\delta(k-m) \tag{16}$$

and the one-dimensional wavenumber spectrum is

$$\Gamma_s(k) = < \hat{S}(\pi/2, k, t)\hat{S}(\pi/2, k, t)^* >$$

$$= \sum_{n=0}^{90} a_n^2(t)(2n+1) \sum_{m=0}^{n} \frac{\Gamma(n-m+1)}{4\pi\Gamma(n+m+1)}$$

$$\times \left\{ \frac{\Gamma[(n+m+1)/2]}{\Gamma[(n-m)/2+1]} \frac{2^m}{\sqrt{\pi}} \cos[\frac{\pi}{2}(n+m)] \right\}^2 \delta(k-m)$$

$$+ \sum_{n=0}^{90} a_n^2(t)(2n+1) \sum_{m=-n}^{-1} \frac{\Gamma(n-|m|+1)}{4\pi\Gamma(n+|m|+1)}$$

$$\times \left\{ \frac{\Gamma[(n+|m|+1)/2]}{\Gamma[(n+|m|)/2+1]} \frac{2^{|m|}}{\sqrt{\pi}} (-1)^m \right\}^2$$

$$\times \left\{ \cos[\frac{\pi}{2}(n+|m|)] \right\}^2 \delta(k-m)$$

$$= \sum_{n=k}^{90} a_n^2(t)(2n+1) \sum_{m=0}^{n} \frac{\Gamma(n-k+1)}{4\pi\Gamma(n+k+1)}$$

$$\times \left\{ \frac{\Gamma[(n+k+1)/2]}{\Gamma[(n-k)/2+1]} \frac{2^k}{\sqrt{\pi}} \cos[\frac{\pi}{2}(n+k)] \right\}^2$$

$$+ \sum_{n=k}^{90} a_n^2(t)(2n+1) \sum_{m=-n}^{-1} \frac{\Gamma(n-|k|+1)}{4\pi\Gamma(n+|k|+1)}$$

$$\times \left\{ \frac{\Gamma[(n+|k|+1)/2]}{\Gamma[(n+|k|)/2+1]} \frac{2^{|k|}}{\sqrt{\pi}} (-1)^k \cos[\frac{\pi}{2}(n+|k|)] \right\}^2 \tag{17}$$

with the terms in the summation vanishing except for $n + k$ even. Equation (17) is the one-dimensional spectrum consistent with the observed degree variances. (*Wagner and Colombo* [1979] provide a related expression.) The "equator" for which (17) is valid is not the physical equator; rather, it is the equator of the sphere on which the hypothetical isotropic, homogeneous stochastic field would exist. The result in units of square centimeter per cycle per kilometer is displayed in Figure 5a.

It is desirable to extend the spherical harmonic along-track wavenumber spectrum in figure 5a to higher wavenumbers, and this extension is possible because the along-track spatial sampling is at approximately 6 km, yielding a Nyquist cutoff near wavelengths of 12 km. The dashed line in figure 5a displays the global average, one-dimensional wavenumber spectral density from a large number of long arcs around the world and averaged both over arcs and over time. Although the subsatellite tracks are not actually great circles, the wavenumber spectra from true great circles probably do not significantly differ from those in Figure 5a. There is excellent agreement between the directly computed one-dimensional wavenumber spectrum and that inferred from the degree variances in the band of overlapping wavenumbers from about $10^{-4} - 10^{-3}$ cycles/kilometer (wavelengths of 1000–10,000 km). Obtaining this agreement is a severe test of a consistent set of normalizations throughout and shows that the approximate global average isotropy assumption is qualitatively correct. (The
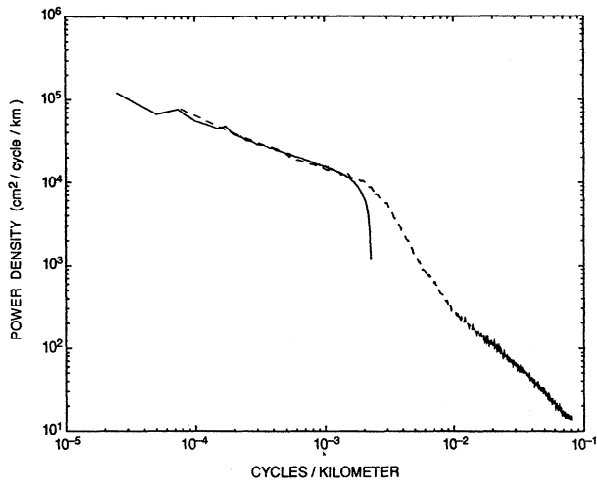
**Figure 5a.** One-dimensional wavenumber spectral density of the variability computed from periodograms along a set of long $(12,700$ km$)$, globally distributed arcs and then averaged (dashed line). The solid line at low wavenumbers is value of the one-dimensional spectrum deduced from (17). See text for a discussion of the deviations of the two curves. The normalization is such that a deterministic unit amplitude sinusoid would produce a power of $1/2$. The conventional spectrum used to infer the extension was not corrected for the remaining tidal energy. The high-wavenumber end has been shaded to indicate uncertainty over the relative noise contribution.

result from (17) was a uniform factor of 1.2 higher than that from the along-track values; the discrepancy is believed to be the aliasing, described above, of the spherical harmonic fit.) Note that the along-arc estimates were not corrected for residual tidal errors and undersample the intense boundary current regions because few long tracks are available in the western boundary areas.

The values inferred from the degree variances drop below those from the along-track values near 500-km wavelengths and shorter owing to the absence in the gridded data of the energy removed by averaging over $2°$ of latitude and longitude. (Note that spectral components of $n$ higher than 90 contribute energy at all values of $|m| < n$ to the degree variances. These contributions are missing in Figure 5a, leading to the observed drop, but which is apparent only at high wavenumbers because there is a very rapid loss in energy at short scales.)

An approximate analytic fit to the combined wavenumber spectrum shown in Figure 5b is

$$\Gamma_s(k) =$$
$$487k^{-1/2}, \quad 2.5 \times 10^{-5} \le k \le 2.4 \times 10^{-3},$$
$$2.6 \times 10^{-3}k^{-5/2}, \quad 2.4 \times 10^{-3} \le k \le 1.0 \times 10^{-2},$$
$$0.59k^{-4/3}, \quad 1.0 \times 10^{-2} \le k \le 1/12, \qquad (18)$$

and whose integral corresponds to about 8.5 cm rms (the annual cycle energy is partially missed by the fit, accounting for the slight reduction from the total variance of the frequency spectrum). The power laws in

(18) and (10) were chosen to be simple and suggestive; But it would be a mistake to attach any great significance to them except, perhaps, in the lowest wavenumber band. These rules represent a great variety of physically disparate regions with varying physics, and it is unlikely that the power laws can be associated with any specific physical cascade mechanism. It is easy to generate a variety of slopes out of ratios of small integers. The validity of the spectrum at the high wavenumber end, approximately proportional to $k^{-4/3}$, is not clear to us and is further discussed below.

The half-power point in the spectrum (18) lies near $k = 1/890$ km; that is, about half the variability in surface potential energy occurs on wavelengths longer than about 1000 km. Although superficially different, the high-wavenumber behavior in Figures 5a and 5b is consistent with results from regional analyses (e.g., D. Stammer, Regional characteristics of oceanic variability estimated from TOPEX/POSEIDON altimeter measurements, manuscript in preparation, 1995), whose spectra have high-wavenumber slopes ranging from $k^{-3}$ to $k^{-5}$ in low- and high-energy areas, respectively. As discussed by *Stammer and Böning* [1992], the distinct dependence on latitude of the shortest important scale leads to a "filling in" of the spectrum by the regions of high energy.

For some purposes, the piecewise rule (18), with its discontinuous first derivatives, is awkward. Another approximation to the spectrum is the Padé form (in units of square centimeter per cycle per kilometer)

$$\Gamma_s(k) = \frac{a_0 - a_1k + a_2k^2}{1 + b_1k - b_2k^2 + b_3k^3 + b_4k^4}, \qquad (19)$$

for the wavenumber range $2.5 \times 10^{-5} \le k \le 1/12$ cycle/kilometer. In (19), $a_0 = 1.1 \times 10^5$, $a_1 = 2.8 \times 10^7$, $a_2 = 2.1 \times 10^9$, and $b_1 = 7.0 \times 10^3$, $b_2 = 2.3 \times 10^6$, $b_3 = 41.6 \times 10^8$, and $b_4 = 1.8 \times 10^{10}$. (The specific numbers appearing in these Padé fits are very sensitive both to the order chosen and the way in which the fitting was weighted. The general shapes are, however, stable.)
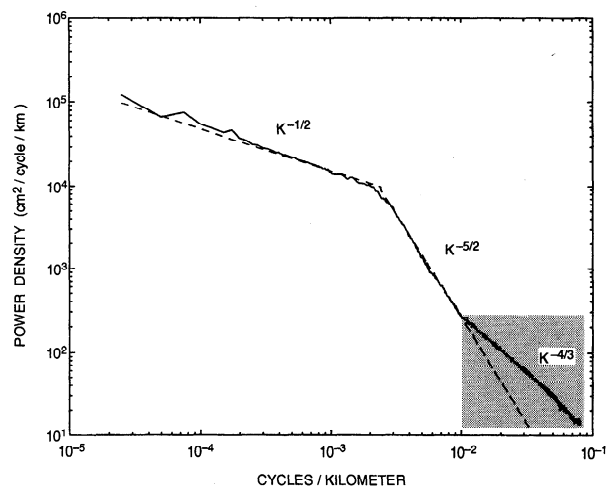


**Figure 5b.** Composite wavenumber spectrum and the piecewise constant power laws in (18). Again, the high-wavenumber end is of uncertain validity.

A geographical depiction of the wavenumber distribution of the variability analogous to that shown in Plates 3a and 3b for the frequency distribution is not rigorously possible because Parseval's theorem in wavenumber space applies only on the global average, not at any particular point. That is, the temporal variance at a fixed location is not the sum of the variances in different wavenumber bands, rather, it is the variance of the sum of those bands. Nonetheless, a qualitative understanding of the wavelength distribution of the variability in geographical coordinates can be obtained. Plate 4a depicts the variance geographically, when the fields $S(\theta, \lambda, t)$ are reconstructed from the expansion to degree 40 only, all wavelengths shorter than about 1000 km being removed. The pattern is similar to the amplitude of the seasonal cycle as depicted by *Stammer and Wunsch* [1994, Plate 4], suggesting that much of the long-wavelength variability (at least on periods shorter than 2 years) lies in the annual cycle, and much of which is local steric effects. Extended patches of low-wavenumber variability in the tropics are also evident. The corresponding estimate of high-wavenumber variability (wavelengths shorter than about 1000 km) was obtained by subtracting the variance shown in Plate 4a from those in Plate 2, so that the high wavenumbers present in the along-track variability are retained, and is shown in Plate 4b. In comparison to the total in Plate 2, the areas of minimum eddy variability now show amplitudes barely exceeding 3 cm rms. High eddy variability generally remains associated with the major current systems, with the Circumpolar Current emerging more clearly as a region of short-scale variability. Plate 4c shows the fraction of high-wavenumber variability, relative to the total variability. The most conspicuous feature is the contrast between the tropics and the higher latitudes, with the short-scale dominance in the southern hemisphere being consistent with the very weak annual cycle there.

Features such as the high-wavenumber extension of the Gulf Stream/North Atlantic Current system are associated with long timescales (Plate 4c), consistent with dominantly baroclinic motions. A similar behavior appears to be associated with the Kuroshio Extension. In contrast, the high-latitude North Pacific and some other areas show a dominance of low wavenumbers at high frequencies, suggestive of barotropic motions. A discussion such as this clearly leads one into a series of interesting regional issues, in which inferences can be made about the internal oceanic motions; but as our goal here is primarily to focus on the global averages, we will leave the regional discussion to future work.

The spectrum of the surface slope obtained by multiplying the results of Figure 5 by $k^2$ is shown in Figure 6. The energetic part of the spectrum has a weak bimodal character; one peak exists near 400-km wavelength (scale near 100 km, if it is defined as 1/4 of a wavelength) and a second peak near the high-wavenumber cutoff around 20 km wavelength which is a consequence of the $-4/3$ power law regime in (18). The longer-wavelength peak occurs near the break in the elevation

spectrum from the $-1/2$ to $-5/2$ power laws, while the significance of the increase in energy toward the highest resolved wavenumber is unclear. In a regional study, extending the results of this paper, Stammer (manuscript in preparation, 1995) shows that this peak is associated, at least in part, with small-scale energy in the intense boundary currents and high latitudes, while part of it is probably system noise. Numerical experiments [e.g., *McWilliams and Chow*, 1981] indicate that the kinetic energy spectrum should decay monotonically from the scale at which energy is input to variability by baroclinic instability; but those models do not contain the equivalent of the intense boundary currents, which contain much of the short spatial-scale variability seen in Plate 4b and tend to have viscous cutoffs at high wavenumbers. So the rise toward the high-wavenumber cutoff could be real nearly geostrophic motions. Note that the total sea level variability in this band is only 2.2 cm rms.

On the other hand, *Rodríguez and Martin* [1994] show that the standard data reduction algorithm is likely removing real energy in the highest-wavenumber band (wavelengths 6-60 km) by improper handling of the details of the returning radar pulse within the altimeter. According to their estimates, the energy at the shortest wavelengths in Figure 6 is about 40% too low. Applying their correction renders the $-4/3$ region closer to the spectrum of white noise but remaining somewhat red in character. Were the spectrum actually white in this wavenumber band, we would normally claim that the "least count" noise of the system had been reached and that no signal could be perceived. Another complicating possibility is residual aliasing of high-frequency motions, such as internal waves, not normally regarded as an element in sea surface variability. At the 2-cm level, movement of the sea surface by internal waves can be significant, and these motions occur on wavelengths of about 150 km and shorter. (*Wunsch and Gill* [1976] estimate that in the tropical thermocline a first vertical mode internal wave displacement of about 8 m produces a 1-cm vertical movement of the sea surface.) Because the interpretation of this $-4/3$ regime is at present so obscure, we have shaded the $k^{-4/3}$ portion of the surface variability spectrum and the corresponding area of the slope spectrum to indicate our uncertainty.

The slope spectrum is very similar to spectra of geostrophic velocity which were computed but are not displayed here because such spectra cannot be simply carried across the equatorial region. The slope spectrum is a good indicator of the visual structures captured by the eye in Plate 1.

If the high-wavenumber extension to the one-dimensional spectrum shown in Figures 5a and 5b is assumed correct, (17) can be used in the opposite sense to infer the degree variances $\Gamma_d(n)$ above $n = 90$. To produce these estimates, $\Gamma_s(k)$ was taken from the values shown in Figures 5a and 5b, resulting in the dashed curve in Figure 4, which now represents an estimate of the global variability degree variances ranging from 40,000- to about 40-km wavelength. The estimate was
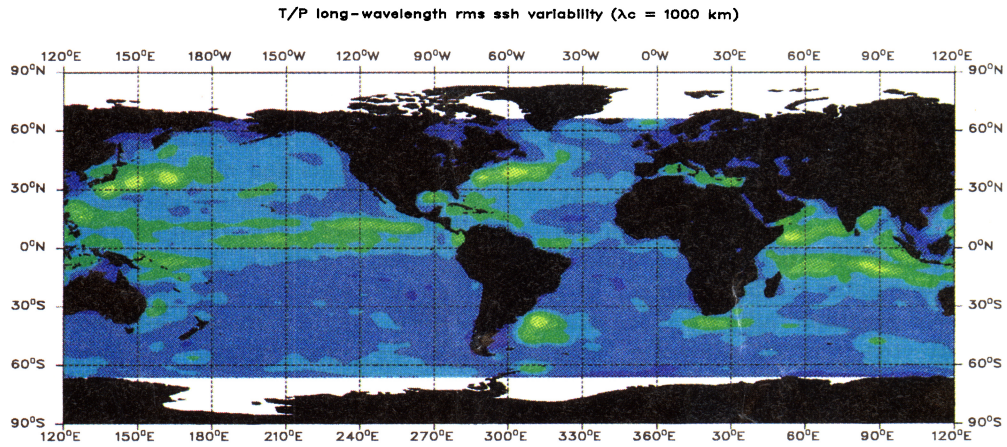
**Plate 4a.** The rms variability of surface topography when all wavelengths shorter than about 1000 km are removed. Scale is cm.
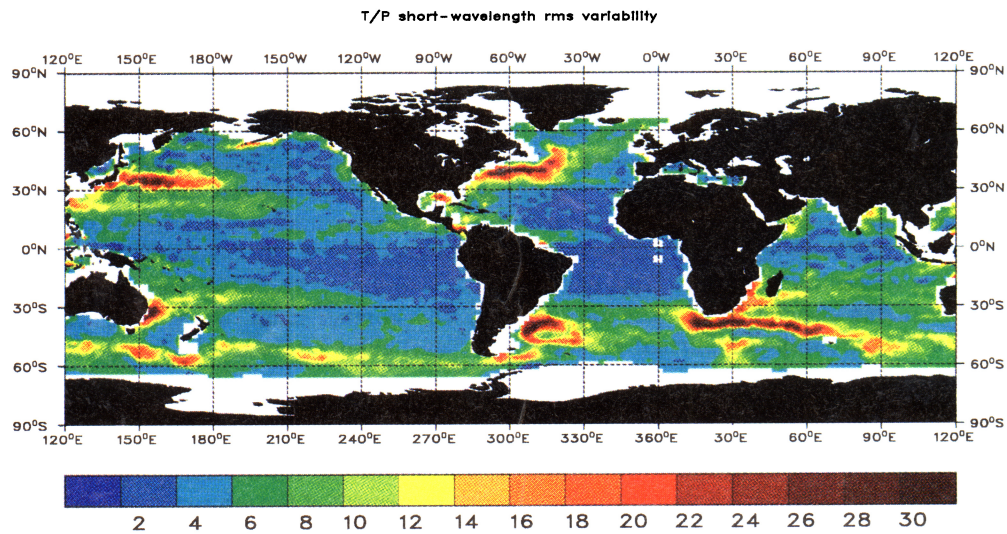


**Plate 4b.** RMS variability of surface topography when the variance corresponding to Plate 4a is subtracted from the variance in Plate 2 to produce an approximate estimate of the high-wavenumber contributions.
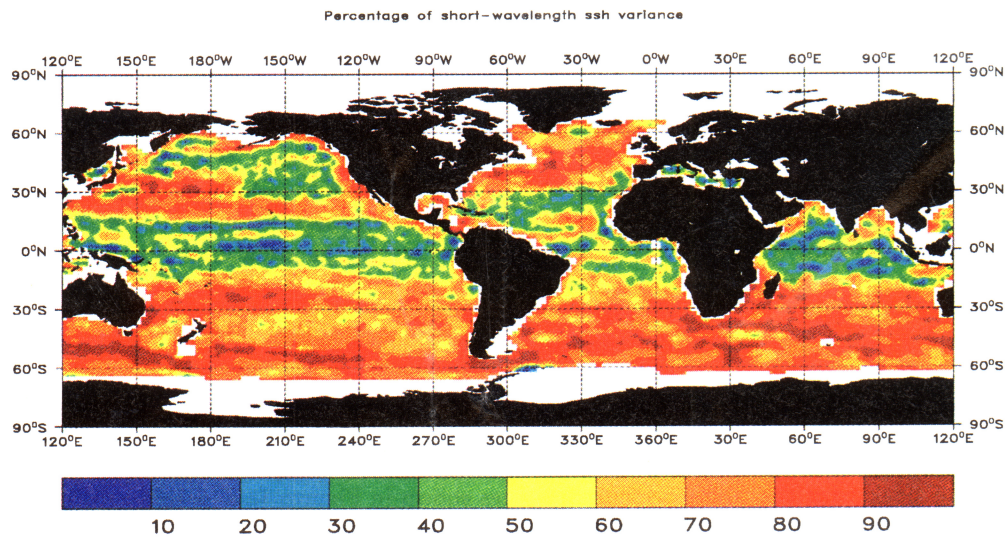


**Plate 4c.** Fraction of the variance corresponding to Plate 4b, relative to the total variance.
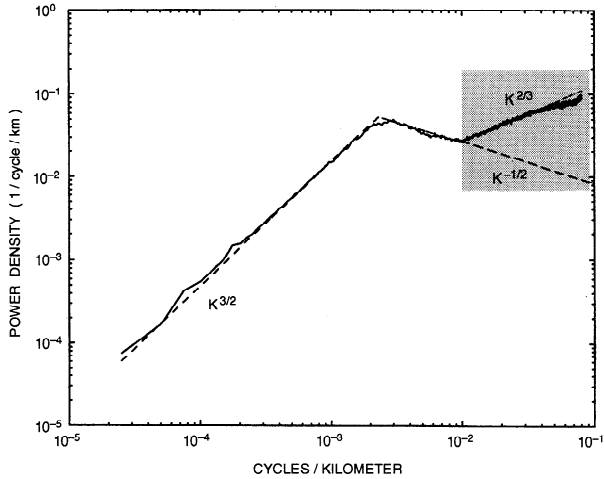
**Figure 6.** Surface slope spectra inferred from the composite spectrum shown in Figure 5b (solid line) and the piecewise constant power laws consistent with (18) (dashed line). The validity of the final increase at the highest wavenumbers is not clear with the dashed line possibly being more accurate. Area is shaded to indicate the uncertainty here.

not carried all the way to the hypothetically possible limit of about 12-km because in addition to the uncertainty of the validity of the spectrum there, a 12 km wavelength corresponds to spherical harmonic degree greater than 3300, thus leading to a set of simultaneous equations for the degree variances which was too large for an ordinary workstation computer. The upturn at the highest values of $n$ is an artifact of the high-wavenumber cutoff in the along-track spectrum used; but it is a reasonable inference that simple extrapolation of the straight line portion of the curve in Figure 4 is a good approximation at the very high degrees. An approximate analytic expression for the degree variances is

$$a_n^2 \times (2n+1) =$$
$$\frac{19.1 - 8.9 \times 10^{-2} n + 2.2 \times 10^{-4} n^2}{1 + 9.4 \times 10^{-2} n - 1.1 \times 10^{-4} n^2 + 4.3 \times 10^{-6} n^3}$$

$$(20)$$

(There is some sensitivity in inverting the wavenumber spectrum for degree variances. When the estimate shown in Figure 4 was calculated not from the numerical values but from the piecewise analytical expression (18) for $\Gamma_s(k)$, the result was a curve with cusps, apparently connected with the slope discontinuities in the one-dimensional expression, and a negative degree variance for $n = 0$. These cusps and negative values disappeared when (19) was used instead. The uncertainty noted above about the actual slope at the very highest wavenumbers in Figure 6 is negligible here, as so little energy is present in those scales.)

### The Frequency-Wavenumber Spectrum

Equation (17) was applied above to the total degree variances; but it can be applied also to the degree variances as a function of frequency, thus producing a two-

dimensional frequency-wavenumber spectrum where the spatial coordinate is once again measured along track, with the result depicted in Figure 7a. The spectrum was cut off at wavelengths shorter than about 500 km because of the removal of energy beyond that owing to the gridding. The annual peak is again conspicuous.

A reasonable analytic fit to the figure can be obtained from the products of the proposed separate frequency and wavenumber spectra. Because of the piecewise form in which $\Gamma_t(\sigma), \Gamma_s(k)$ have been written, there are six separate regimes, and the result can be written in a number of ways, one of which is

$$\Psi(k, \sigma) = 2.9 \times 10^{-7}$$
$$\times \left\{ \sigma^{-1}, 0 \leq \sigma \leq 5 \times 10^{-2}, 0.46 \sigma^{-2}, 5 \times 10^{-2} \leq \sigma \right\}$$
$$\times \left\{ \begin{array}{l} k^{-1/2}, 2.5 \times 10^{-5} \leq k \leq 2.4 \times 10^{-3}, \\ 5.3 \times 10^{-6} k^{-5/2}, 2.4 \times 10^{-3} \leq k \leq 1.0 \times 10^{-2}, \\ 1.2 \times 10^{-3} k^{-4/3}, 1.0 \times 10^{-2} \leq k \leq 1/12, \end{array} \right\}$$

$$(21)$$

where units are cm$^2$ cycle$^{-1}$ d$^{-1}$ cycle$^{-1}$ km$^{-1}$. The result is shown in Figure 7b. The fit is inadequate at the annual peak, and a quantitative description of that structure and the spectrum at longer periods awaits a longer record.

### 4. Spatial Covariance

For some purposes, e.g., surface mapping and spatial correlation calculations, it is useful to have the spatial covariance function $C$. Define

$$C(\theta, \Delta\theta, \Delta\lambda, t)$$
$$= \ < S(\theta + \Delta\theta, \lambda + \Delta\lambda, t) S(\theta, \lambda, t)^* >$$
$$= \sum_{n=0}^{N} \sum_{m=-n}^{n} \sum_{p=0}^{N} \sum_{q=-p}^{p} < \alpha_{nm}(t) \alpha_{pq}^*(t) >$$
$$\times \ Y_{nm}(\theta + \Delta\theta, \lambda + \Delta\lambda) Y_{pq}(\theta, \lambda)^*$$
$$= \sum_{n} a_n^2(t) \sum_{m=-n}^{n} Y_{nm}(\theta + \Delta\theta, \lambda + \Delta\lambda)$$
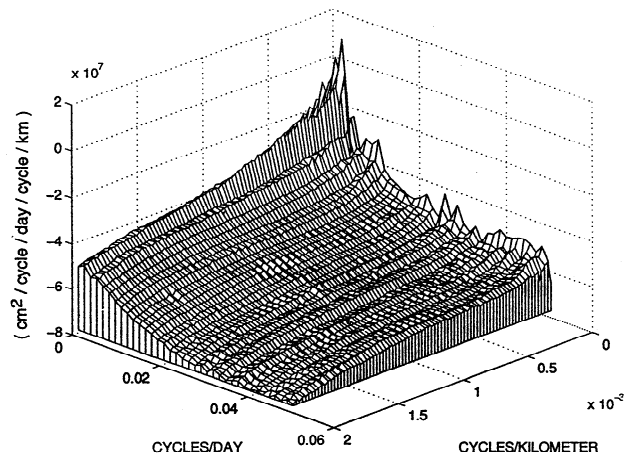$$\times \ Y_{nm}(\theta, \lambda)^*$$

$$(22)$$



**Figure 7a.** Frequency-wavenumber power density spectrum of the global ocean as inferred from the spherical harmonic fit converted to along-track coordinates. (No averaging was done.) The annual peak is the most conspicuous feature.

But the addition theorem of spherical harmonics [e.g., *Jackson*, 1962, p. 68) asserts that

$$P_n(\cos\gamma) = \frac{4\pi}{2n+1}\sum_{m=-n}^{n}Y_{nm}(\theta+\Delta\theta,\lambda+\Delta\lambda)Y_{nm}(\theta,\lambda)^* \tag{23}$$

where $\cos\gamma = \cos\theta\cos(\theta+\Delta\theta)+\sin\theta\sin(\theta+\Delta\theta)\cos\Delta\lambda$. Hence (22) can be written, using the lack of dependence on $m$ of the coefficients,

$$C(\theta,\Delta\theta,\Delta\lambda,t) = \sum_{n=0}^{90}a_n^2(t)\frac{2n+1}{4\pi}P_n(\cos\gamma) \tag{24}$$

If this function is in turn expanded in $Y_{nm}$ to produce a "spectrum," one uses

$$Y_{n0}(\gamma,\phi) = \sqrt{\frac{2n+1}{4\pi}}P_n(\cos\gamma) \tag{25}$$

and
the power in each degree will be $a_n^2(t)\sqrt{(2n+1)/4\pi}$. Setting $\Delta\theta = \Delta\lambda = 0, \cos\gamma = 1$, and hence the mean square value is

$$< S(\theta,\lambda,t)S(\theta,\lambda,t)^* >$$
$$= \sum_{n=0}^{90}a_n^2(t)\frac{2n+1}{4\pi}P_n(\cos 0)$$
$$= \sum_{n=0}^{90}a_n^2(t)\frac{2n+1}{4\pi} = C(\theta,0,t) \tag{26}$$

independent, in this homogeneous isotropic regime, of position. From the "Fourier" form (12), the mean-square value for any $\lambda$ is,

$$< S(\pi/2,\lambda,t)S(\pi/2,\lambda,t)^* >$$
$$= \sum_{n=0}^{90}\sum_{m=-n}^{n}\sum_{p=0}^{90}\sum_{q=-p}^{p} < \alpha_{nm}\alpha_{pq}^* >$$
$$\times \ Y_{nm}(\pi/2,\lambda)Y_{pq}(\pi/2,\lambda)^*$$
$$= \sum_{n=0}^{90}\sum_{m=-n}^{m}a_n^2(t)|Y_{nm}(\theta,\lambda)|^2$$
$$= \sum_{n=0}a_n^2(t)\frac{2n+1}{4\pi}, \tag{27}$$

where the last step uses the addition theorem (23) with $\gamma = 0, P_n(1) = 1$. Equation (27) is necessarily the same as (26). Because of the special role of the poles in spherical coordinates, $C(\theta,\Delta\theta,\Delta\lambda,t)$ depends upon $\theta$, in contrast to the situation for a homogeneous process on the plane.

For fixed $t$, (24), along with the analytical approximation (20), can be used, e.g., for objective mapping. It can also be readily generalized to account for temporal lags as well as spatial separations, but we will omit displaying the formal expression here, as it is implicit in the formulas already given.
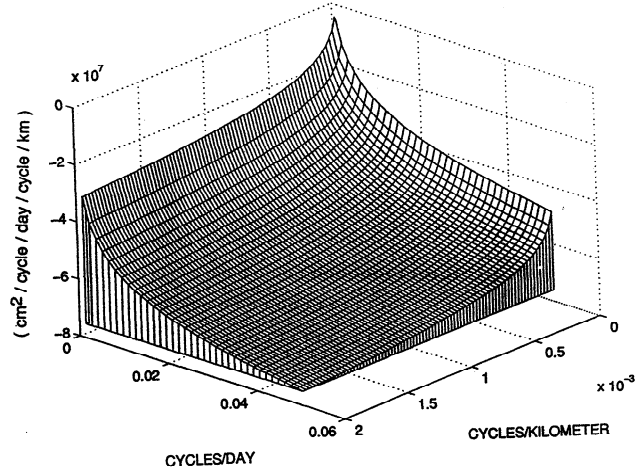


**Figure 7b.** Analytical form of Figure 7a, as expressed in (21) .

Similarly, all of the along-track spectra correspond to spatial (and/or temporal) covariances, computable as the cosine transforms of the one-dimensional spectra. Of particular interest is the covariance of the slope spectrum in Figure 6. For present purposes we assume that the $k^{-5/2}$ region of $\Gamma_s(k)$ extends to $k = \infty$, possibly underestimating the high wavenumber energy and thus slightly distorting the covariance at small lags. Define

$$C(\tau) = 2\int_o^\infty k^2\Gamma_s(k)\cos(2\pi k\tau)dk. \tag{28}$$

The result is expressible in terms of Fresnel integrals, but we display only its graph in Figure 8. The infinity at zero lag is integrable; there is a first zero crossing near 54 km and a decaying sinusoid beyond. Large-lag oscillations are generated by the abrupt change in slope in $\Gamma_s(k)$ at 400 km. This result should be close to the one-dimensional global average transverse geostrophic velocity covariance.

## 5. Using the Results

The results are best regarded as basic descriptive physical oceanography, raising fundamental dynamical and theoretical issues of why these particular spectral forms are displayed by the ocean. Apart from such theoretical issues, the results can be exploited in a number of ways. Although their use is mainly left to future papers, we offer three examples.

1. Ordinary tide gauges represent an entirely different method for observing sea level variability. One seeks to compare and to combine these measurements. This recipe was carried out by *Wunsch* [1991] for GEOSAT measurements, but the work was hindered by the difficulties in determining how well the pointwise measurements at the tide gauges should agree with the spatially averaged altimetric ones. Expression (18) now permits an answer to that question in the global average: integrating (18) from $k = 1/200$ km (approximating a $2°$ average) to $k = 1/12$ km produces about $(3\text{ cm})^2$ as an estimate of the mean square energy removed by the
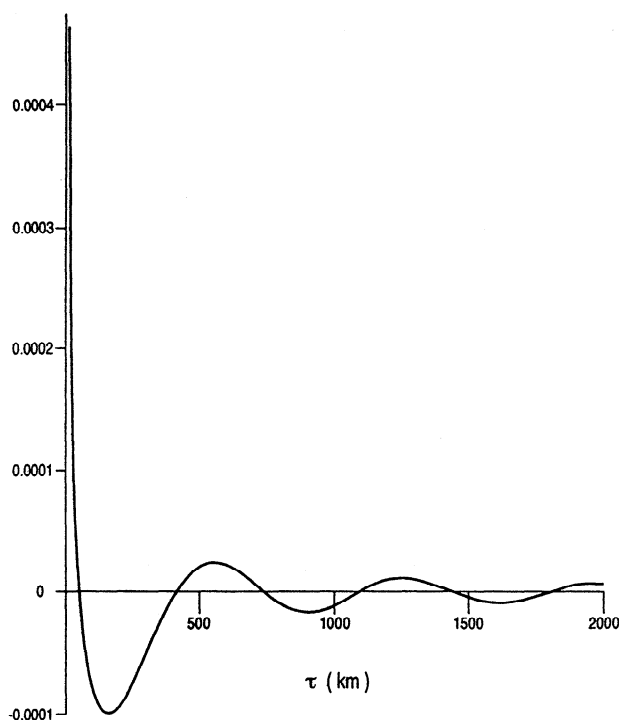
**Figure 8.** Spatial covariance, normalized to unity, of the along-track slope spectrum; modified to omit the high wavenumber increase and which should be nearly proportional to the transverse geostrophic velocity. The nearly white character of the slope spectrum generates the near-delta function at the origin. Approximate mean square geostrophic kinetic energy is 500 cm/s$^2$, which sets the scale for the figure.

averaging. For any particular gauge, deviations from this value are to be expected; but this value provides a default a priori value which would then be modified in a simple adaptive method which tracked the actual altimeter –tide gauge differences through time, a calculation to be presented in a subsequent paper.

2. The sampling properties of altimetric satellites must be understood in the context of oceanic variability [e.g., *Wunsch*, 1989]. Some debate has occurred concerning the desirability of orbits such as that occupied by GEOSAT, in which the ground track repeated every 17 days versus that of TOPEX/POSEIDON repeating every 10 days. We can now answer the question of how much energy in the global average is aliased by the 17-day repeat relative to the 10-day repeat; it is

$$\int_{s=1/34d}^{s=1/20d} \Gamma_t(s)ds \approx (1.9)^2 \text{ cm}^2 \qquad (29)$$

which is not insignificant and which will be much higher in certain regions. (The 10-day TOPEX/POSEIDON repeat cycle was chosen in part because it appeared that at periods shorter than about 20 days, the spectral drop-off in sea level variability became quite steep, thus minimizing the aliasing from shorter periods; but some residual temporal aliasing is inevitable.) The 17-day repeat ground track is denser on the surface than

is the 10-day one, permitting contemplation of the removal of the aliased energy by wavenumber filtering; although this is a difficult problem, given the irregular data distributions. However, with knowledge of the full-frequency wavenumber spectra, such filters could, in principle, be designed.

3. *Brown et al.* [1975] and *Filloux et al.* [1991] have reported estimated spectral densities from seafloor pressure gauges; the former from southwest of Bermuda and the latter from north of Hawaii. In the band of timescales that overlap their estimates with ours, from about 20 to 100 days, their results suggest that the energy levels on the seafloor are approximately the same as seen from the altimeter on the global average; suggesting that at these rather short periods in these particular locations, the motions are largely barotropic; as theory implies high-frequency forced motions should be. (The pressure records were too short to make estimates at longer periods.)

## 6. Final Comments

There is much more to be done along the lines outlined here, work which will be described in future publications. As an example, one seeks to extract directional properties from the data, i.e., a determination of the fraction of the energy propagating westward, northward, etc. The problem of the vertical partitioning of the energy can be understood, both through the frequency structure of the spectra at fixed wavenumber and through the comparison with in situ observations, such as those of *Filloux et al.* [1991] and *Brown et al.* [1975]. Comparison of the regional variations of the spectra to the global means is a determinant of local physics, and a regionalized version of these results is in preparation. Through comparisons and combinations with the tide gauge results, a much tighter bound on the accuracy of present estimates of global secular trends should become possible. The frequency/wavenumber spectrum implies coherence scales between physically separated measurements as a function of frequency, and these predictions need to be tested directly against observations.

The close agreement between the spectra derived from the spherical harmonic analysis of the gridded data and that from the "raw" along-track values gives us confidence in the results and suggests there are no obvious problems of aliasing of the gridded values by high-wavenumber variability, nor of serious anisotropy aliasing the along-track analyses. The one-dimensional analyses of the raw data are far simpler than use of the spherical harmonics and will probably be the focus of most future work; but the spherical harmonic approach better lends itself to global-scale three-dimensional (frequency/wavenumber) analysis and will continue to play a role.

## Appendix A: The Spherical Harmonics

Define the degree $n$ Legendre functions as

$$P_n(z) = \frac{1}{2^n n!} \frac{d^n}{dz^n} (z^2 - 1)^n \qquad (A1)$$

(Rodrigues's formula) with the associated Legendre functions defined as

$$P_{nm}(z) = (-1)^m (1 - z^2)^{m/2} \frac{d^m}{dz^m} P_n(z) \qquad (A2)$$

for $0 \le m \le n$, and

$$P_{nm}(z) = (-1)^{|m|} \frac{(n - |m|)!}{(n + |m|)!} P_{n|m|}(z) \qquad (A3)$$

for $-n \le m \le -1$. Then the spherical harmonics are

$$Y_{nm}(\theta, \lambda) = \sqrt{\frac{(2n + 1)(n - m)!}{4\pi(n + m)!}} P_{nm}(\cos\theta) e^{im\lambda} \qquad (A4)$$

for $0 \le m \le n$, and

$$Y_{nm}(\theta, \lambda) = (-1)^{|m|} Y_{n|m|}^*(\theta, \lambda) \qquad (A5)$$

for $-n \le m \le -1$. The result is fully normalized over the sphere

$$\int_0^{2\pi} d\lambda \int \sin\theta Y_{nm}(\theta, \lambda) Y_{n'm'}^*(\theta, \lambda) d\theta = \delta_{nn'}\delta_{mm'} . (A6)$$

# References

Brown, W., W. Munk, F. Snodgrass, B. Zetler, and H. Mofjeld, MODE bottom experiment, *J. Phys. Oceanogr.*, **5**, 75-85, 1975.

Filloux, J. H., D. S. Luther, and A. D. Chave, Long-term seafloor mesurements of water pressure: Normal modes and infragravity waves, paper presented at 20th General Assembly, Int. Union of Geod. and Geophys., Vienna, 1991.

Fu, L.-L., E. J. Christensen, C. A. Yamarone, M. Lefebvre, Y. Ménard, M. Dorrer, and P. Escudier, TOPEX/POSEIDON mission overview, *J. Geophys. Res.*, **99**, 24,369-24,382, 1994.

Garrett, C. J. R., and W. H. Munk, Space-time scales of internal waves, *Geophys. Fluid Dyn.*, **3**, 225-264, 1972.

Haines, G. V., Spherical cap harmonic analysis, *J. Geophys. Res.*, **90**, 2583-2591, 1985.

Hobson, E. W., *The Theory of Spherical and Ellipsoidal Harmonics*, 500 pp., Chelsea, New York, 1955.

Hwang, G., Spectral analysis using orthonormal functions with a case study in the sea surface topography, *Geophys. J. Int.*, **115**, 1148-1160, 1993.

Jackson, J. D., *Classical Electrodynamics*, 641 pp., John Wiley, New York, 1962.

Jones, R. H., Stochastic processes on a sphere as applied to meteorological 500-millibar forecasts, in *Time Series Analysis*, edited by M. Rosenblatt, pp. 119-124, John Wiley, New York, 1963.

Kaula, W. M., Theory of statistical analysis of data distributed over a sphere, *Rev. Geophys.*, **5**, 83-107, 1967.

King, C., D. Stammer, and C. Wunsch, *The CMPO/MIT TOPEX/POSEIDON altimetric data set, Rep. 30*, 33 pp. plus color plates, Cent. for Global Change Sci., Mass. Inst. of Technol., Cambridge, 1994 .

LeTraon, P. Y., J. Stum, J. Dorandeu, P. Gaspar, and P.

Vincent, Global statistical analysis of TOPEX and POSEIDON data, *J. Geophys. Res.*, **99**, 24,619-24,631, 1994.

Ma, X. C., C. K. Shum, R. J. Eanes, and B. D. Tapley, Determination of ocean tides from the first year of TOPEX/POSEIDON altimeter measurements, *J. Geophys. Res.*, **99**, 24,809-24,820, 1994.

McWilliams, J. C. and H. H. S. Chow, Equilibrium geostrophic turbulence, 1, A reference solution in a $\beta$-plane channel, *J. Phys. Oceanogr.*, **11**, 921-949, 1981.

Munk, W. H. and D. E. Cartwright, Tidal spectroscopy and prediction, *Philos. Trans. R. Soc. London A*, **259**, 533-581, 1966.

Nerem, R. S., Measuring global mean sea level variations using TOPEX/POSEIDON altimeter data, *J. Geophys. Res.*, this issue.

Richman, J.G., C. Wunsch and N.G. Hogg, Space and time scales and mesoscale motion in the sea. *Rev. Geophys.*, **15**, 385-420, 1977.

Rodríguez, E., and J. M. Martin, Assessment of the TOPEX altimeter performance using waveform retracking, *J. Geophys. Res.*, **99**, 24,957-24,970, 1994.

Stammer, D., and C. Böning, Mesoscale variability in the Atlantic Ocean from Geosat altimetry and WOCE high-resolution numerical modeling, *J. Phys. Oceanogr.*, **22**, 732-752, 1992.

Stammer, D., and C. Böning, Generation and distribution of mesoscale eddies in the North Atlantic Ocean, in *Warm Water Sphere of the North Atlantic Ocean*, edited by W. Krauss, Gebrüder Bornträger, Berlin, in press, 1995.

Stammer, D., and C. Wunsch, Preliminary assessment of the accuracy and precision of TOPEX/POSEIDON altimeter data with respect to the large-scale ocean circulation, *J. Geophys. Res.*, **99**, 24,584-24,604, 1994.

Stegun, I. A., Legendre functions, in *Handbook of Mathematical Functions*, edited by M. Abramowitz and I. A. Stegun, pp. 331-354, Dover, Mineola, N. Y., 1965.

Swartztrauber, P. N., On the spectral approximation of discrete scalar and vector functions on the sphere, *SIAM J. Numer. Anal.*, **16**, 934-949, 1979.

Swartztrauber, P. N. and J. C. Adams, Spherepack (A model development facility), internal report, Nat. Cent. for Atmos. Res., Boulder, Colo., 1987.

Thompson, W., and P. G. Tait, *Treatise on Natural Philosophy*, Parts 1 and 2, rev. ed., Cambridge Univ. Press, New York, 1912. (Reprinted as *Principles of Mechanics and Dynamics*, Dover, Mineola, N.Y., 1962.)

Wagner, C. A., and O. L. Colombo, Gravitational spectra from direct measurements, *J. Geophys. Res.*, **84**, 4699-4712, 1979.

Wunsch, C., Bermuda sea level in relation to tides, weather, and baroclinic fluctuations, *Rev. Geophys.*, **10**, 1-49, 1972.

Wunsch, C., Sampling characteristics of satellite orbits, *J. Atmo. and Oceanic Tech.*, **6**, 891-907, 1989.

Wunsch, C., Global-scale sea surface variability from combined altimetric and tide gauge measurements, *J. Geophys. Res.*, **96**, 15,053-15,082, 1991.

Wunsch, C. and A. E. Gill, Observations of equatorially trapped waves in Pacific sea level variations, *Deep Sea Res.*, **23**, 371-390, 1976.

Yaglom, A. M., Second-order homogeneous random fields, Proceedings of *Fourth Berkeley Symposium on Mathematics and Statistics Probability*, vol. 2, pp. 593-622, Univ. of Calif. Press, Berkeley, 1961.

D. Stammer and C. Wunsch, Department of Earth, Atmospheric and Planetary Sciences, Massachusetts Institute of Technology, Cambridge, MA 02139. (e-mail: detlef@lagoon.mit.edu; cwunsch@pond.mit.edu)